

EPINET: A Fully-Convolutional Neural Network Using Epipolar Geometry for Depth from Light Field Images

Changha Shin¹ Hae-Gon Jeon² Youngjin Yoon² In So Kweon² Seon Joo Kim¹
¹Yonsei University ²KAIST

changhashin@yonsei.ac.kr earboll@kaist.ac.kr jeromeyoon@kaist.ac.kr iskweon@kaist.ac.kr seonjookim@yonsei.ac.kr

Abstract

Light field cameras capture both the spatial and the angular properties of light rays in space. Due to its property, one can compute the depth from light fields in uncontrolled lighting environments, which is a big advantage over active sensing devices. Depth computed from light fields can be used for many applications including 3D modelling and refocusing. However, light field images from hand-held cameras have very narrow baselines with noise, making the depth estimation difficult. Many approaches have been proposed to overcome these limitations for the light field depth estimation, but there is a clear trade-off between the accuracy and the speed in these methods. In this paper, we introduce a fast and accurate light field depth estimation method based on a fully-convolutional neural network. Our network is designed by considering the light field geometry and we also overcome the lack of training data by proposing light field specific data augmentation methods. We achieved the top rank in the HCI 4D Light Field Benchmark on most metrics, and we also demonstrate the effectiveness of the proposed method on real-world light-field images.

1. Introduction

Light field cameras collect and record light coming from different directions. As one of the most advanced techniques introduced in the area of computational photography, the new hand-held light field camera design has a broad impact on photography as it changes how images are captured and enables the users to alter the point of view or focal plane after the shooting.

Since the introduction of the camera array system [38], many approaches for making compact and hand-held light field cameras have been proposed like the lenslet-based cameras [25, 3, 2, 26], which utilize a micro-lens array placed in front of the imaging sensor. Images captured from the lenslet-based cameras can be converted into multi-view images with a slightly different view point via geometric

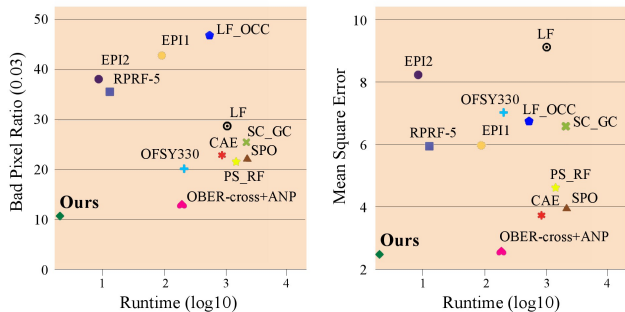


Figure 1. Comparison of the accuracy and the run time of light field depth estimation algorithms. Our method achieved the top rank in the HCI 4D Light Field Benchmark, both in accuracy and speed. Our method is 85 times faster than OBER-cross+ANP, which is a close second in the accuracy ranking.

calibration processes [6, 7]. Thanks to this special camera structure, light field cameras can be used to estimate the depth of a scene in uncontrolled environments. This is one of the key advantages of the light field cameras over active sensing devices [4, 1], which require controlled illumination and are therefore limited to the indoor use.

On the other hand, the hand-held light field cameras have their own limitation. Due to their structure, the baseline between sub-aperture images is very narrow and there exists a trade-off between the spatial and the angular resolution within the restricted image sensor resolution. Various approaches [30, 16, 11, 42, 34, 43] have been introduced to overcome these limitations and acquire accurate depth maps. These methods achieve good performances close to other passive sensor-based depth estimation methods such as the stereo matching, but are less practical due to their heavy computational burden. Although several fast depth estimation methods [37, 15] have been proposed, they lose the accuracy to gain the speed.

In this paper, we introduce a deep learning-based approach for the light field depth estimation that achieves both accurate results and fast speed. Using a convolutional neural network, we estimate accurate depth maps with sub-

pixel accuracy in seconds. We achieved the top rank in HCI 4D Light Field Benchmark¹ [14] on most quality assessment metrics including the bad pixel ratio, the mean square error, and the runtime as shown in Fig. 1.

In our deep network design, we create four separate, yet identical processing streams for four angular directions (horizontal, vertical, left and right diagonal) of sub-aperture images and combine them at a later stage. With this architecture, the network is constrained to first produce meaningful representations of the four directions of the sub-aperture images independently. These representations are later combined to produce higher level representation for the depth estimation.

One problem of applying deep learning for light field depth estimation is the lack of data. Publicly available light field datasets do not contain enough data to train a deep network. To deal with this problem of data insufficiency, we additionally propose a data augmentation method specific for the light field imaging. We augment the data through scaling, center view change, rotation, transpose, and color that are suitable for light field images. Our data augmentation plays a significant role in increasing the trainability of the network and the accuracy of the depth estimation.

2. Related Work

The related works can be divided in two categories: depth from a light field image using optimization approaches and learning-based approaches.

Optimization-based methods. The most representative method for the depth estimation using light field images is the use of the epipolar plane images (EPIs), which consist of 2D slices angular and spatial directions [20, 10]. As the EPI consists of lines with various slopes, the intrinsic dimension is much lower than its original dimension. This makes image processing and optimization tractable for the depth estimation. Wanner and Goldluecke [37] used a structured tensor to compute the slopes in EPIs, and refined initial disparity maps using a fast total variation denoising filter. Zhang *et al.* [43] also used the EPIs to find the matching lines and proposed a spinning parallelogram operator to remove the influence of occlusion on the depth estimation.

Another approach is to exploit both defocus and correspondence cues. Defocus cues perform better in repeating textures and noise, and correspondence cues are robust in bright points and features. Tao *et al.* [30] first proposed a depth estimation that combines defocus and correspondence cues. This approach was later improved by adding shading-based refinement technique in [31] and a regularization with an occlusion term in [34]. Williem and Park [39] proposed a method robust to noise and occlusion. It is equipped with

a novel data cost using an angular entropy metric and adaptive defocus responses.

Many other methods have been proposed to improve the depth estimation from light field image. Heber and Pock [11] proposed a global matching term which formulates a low rank minimization on the stack of sub-aperture images. Jeon *et al.* [16] adopted a multi-view stereo matching with a phase-based sub-pixel shift. The multi-view stereo-based approach enabled the metric 3D reconstruction from a real-world light field image.

These conventional optimization based methods have an unavoidable trade-off between the computational time and the performance. In this paper, we adopt a convolutional neural network framework to gain both the speed and the accuracy.

Learning based methods. Recently, machine learning techniques have been applied to a variety of light field imaging applications such as super-resolution [41, 40], novel view generation [19], single image to a light field image conversion [28], and material recognition [35].

For the depth estimation, Johannsen *et al.* [18] presented a technique which uses EPI patches to compose a dictionary with a corresponding known disparity. This method yielded better results on multi-layered scenes. Heber *et al.* [13] proposed an end-to-end deep network architecture consisting of an encoding and a decoding part. Heber and Pock [12] proposed a combination of a CNN and a variational optimization. They trained a CNN to predict EPI line orientations, and formulated a global optimization with a higher-order regularization to refine the network predictions.

There are still issues in the aforementioned learning based methods. Those methods only consider one directional epipolar geometry of light field images in designing the network [12, 13], resulting in low reliability of depth predictions. We overcome this problem via a multi-stream network which encodes each epipolar image separately to improve the depth prediction. Because each epipolar image has its own unique geometric characteristics, we separate epipolar images into multiple parts to make the deep network to take advantage of the characteristics. Another issue is that the insufficient training data limit the discriminative power of the learned model and lead to over-fitting. In this work, we propose novel data augmentation techniques for light-field images that lead to good results without the over-fitting issue.

3. Methodology

3.1. Epipolar Geometry of Light Field Images

With the insights from previous works, we design an end-to-end neural network architecture for the depth from a light-field image exploiting the characteristics of the light

¹<http://hci-lightfield.iwr.uni-heidelberg.de>

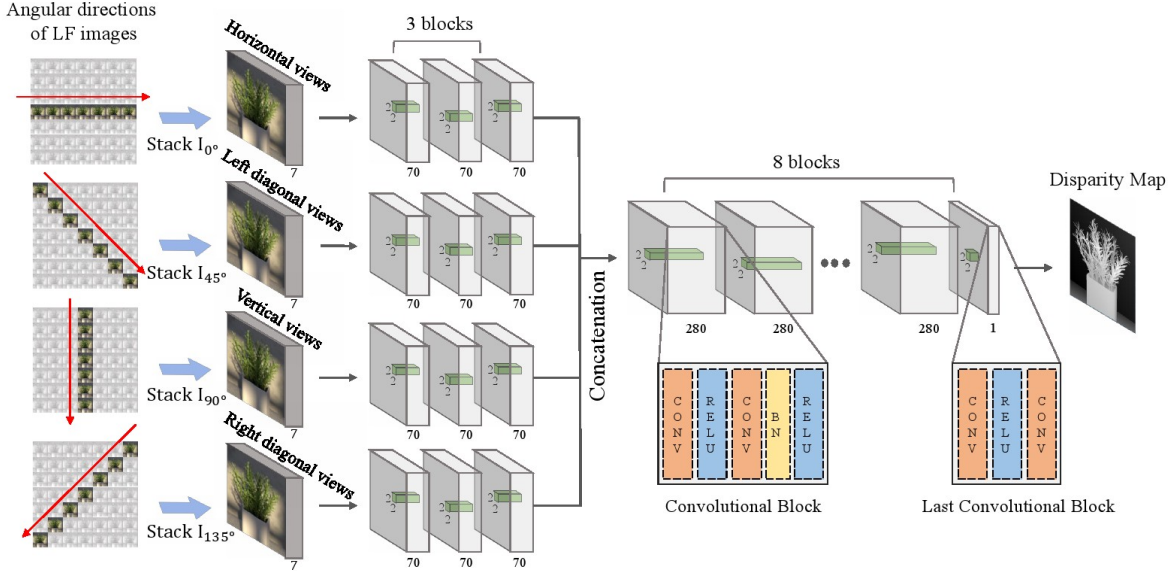


Figure 2. EPINET: Our light field depth estimating architecture.

field geometry. Since the light field image has many angular resolutions in the vertical and the horizontal directions, the amount of data is much bigger than that of a stereo camera. When using all the viewpoints of the light field images as an input data, despite the accurate light field depth results, the computation speed is several hundred times slower than the stereo depth estimation algorithm. To solve this problem, several papers proposed algorithms that only use horizontal or crosshair viewpoints of light field images [37] [18] [43] [29]. Similarly, we propose a depth estimation pipeline by first reducing the number of images to be used for the computation by exploiting the light field characteristics between the angular directions of viewpoints.

The 4D light field image is represented as $L(x, y, u, v)$, where (x, y) is the spatial resolution and (u, v) is the angular resolution. The relationship between the center and the other viewpoints of light field image can be expressed as follows:

$$L(x, y, 0, 0) = L(x + d(x, y) * u, y + d(x, y) * v, u, v), \quad (1)$$

where $d(x, y)$ is the disparity of the pixel (x, y) in the center viewpoint from its corresponding pixel in its adjacent viewpoint.

For an angular direction θ ($\tan \theta = v/u$), we can reformulate the relationship as follows:

$$L(x, y, 0, 0) = L(x + d(x, y) * u, y + d(x, y) * u \tan \theta, u, u \tan \theta) \quad (2)$$

However, the viewpoint index is an integer, so there are no corresponding viewpoints when $\tan \theta$ is non-integer. Therefore, we select images in the direction of four viewpoint angles θ : 0, 45, 90, 135 degrees assuming that the

light field images have $(2N + 1) \times (2N + 1)$ angular resolution.

3.2. Network Design

Multi-stream network. As shown in Fig. 2, we construct a multi-stream networks for four viewpoints with consistent baselines based on Sec. 3.1: horizontal, vertical, left and right diagonal directions. Similar to the conventional optical flow estimation and stereo matching approaches [8, 22], we encode each image stack separately in the beginning of our network. In order to show the effectiveness of the multi-stream architecture, we quantitatively compare our multi-stream network to a single stream network. As shown in Fig. 3, the reconstruction error using the proposed method is about 10 percent lower, even when using the same number of parameters as the one-stream network. With this architecture, the network is constrained to first produce meaningful representations of the four viewpoints.

The multi-stream part consists of three fully convolutional blocks. Since fully convolutional networks are known to be effective architecture for pixel-wise dense prediction [21], we define a basic block with a sequence of fully convolutional layers: 'Conv-ReLU-Conv-BN-ReLU' to measure per-pixel disparity in a local patch. To handle the small baseline of light-field images, we use small 2x2 kernel with stride 1 to measure a small disparity value (± 4 pixels).

To show the effect of different number of streams in the network, we compare the performance of our network with varying number of the streams. Using the same architecture with almost the same number of parameters (5.1M),

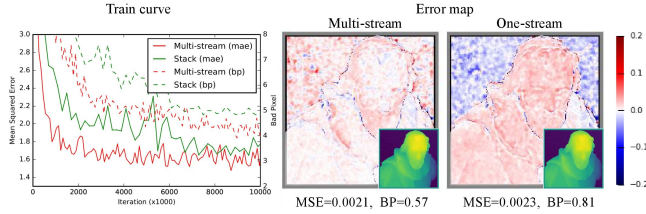


Figure 3. Multi-stream vs one-stream: Test error during training (left), and error map at the 10M iteration (right). In the error map, white color represents lower errors.

Table 1. The effect of the number of viewpoints on performance.

	1-stream	2-streams	4-streams
Input Views			
MSE	2.165	1.729	1.393
Bad pixel ratio (<0.07px)	7.61	5.94	3.87

we compare the difference in performance of our network with different numbers of streams in Table 1. The network with four streams shows the best performance in terms of the bad pixel ratio and the mean square error.

After the multi-stream part, we concatenate all the features from each stream, and the size of the feature becomes four times larger. The merge network consists of eight convolutional blocks that finds the relationships between the features passed through the multi-stream network. The blocks in the merge network have the same convolutional structure with that of the multi-stream network except for the last block. To inferring the disparity values with sub-pixel precision, we construct the last block with a Conv-ReLU-Conv structure.

3.3. Data Augmentation

Although there are some public light-field image datasets, only a few of them have data that are under similar conditions as the real light field image with the ground-truth disparity maps. In this paper, we use the 16 light-field synthetic images containing various textures, materials, objects and narrow baselines provided in [14]. However, 16 light-field images are just not enough to generalize convolutional neural networks. To prevent the overfitting problem, data augmentation techniques are essential. Therefore, we propose a light-field image specific data augmentation technique that preserves the geometric relationship between the sub-aperture images.

Our first strategy is to shift the center view point of the light field image. The synthetic light field dataset that we used has 9×9 views, each with a 512×512 spatial resolu-

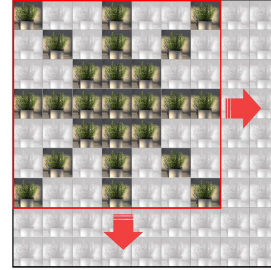


Figure 4. An example of the viewpoint augmentation: $(-1,-1)$ shift.

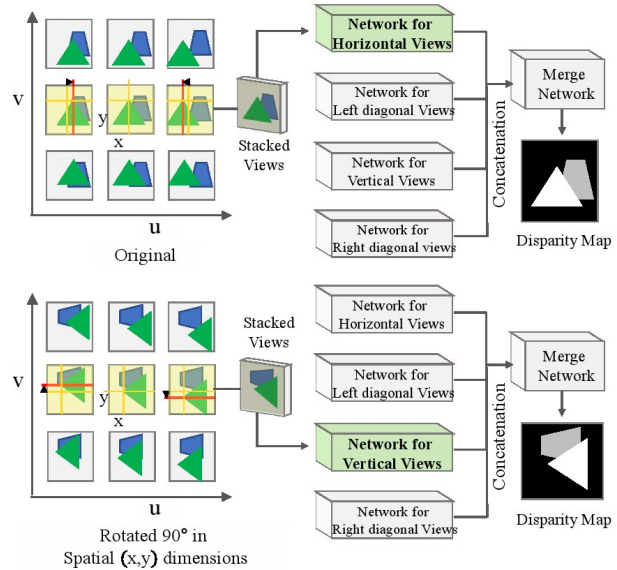


Figure 5. Data augmentation with rotation. When augmenting the data with rotation, we also need to rearrange the connections to put the stacked views into the correct network stream.

tion. As shown in Fig. 4, we select the 7×7 views and disparity image of its center view to train our network. By shifting the center view, we can get nine times more training sets through this view-shifting strategy. To validate the performance according to the number of viewpoints and the view-shifting augmentation, we compare performances of the networks using 3×3 , 5×5 , 7×7 , and 9×9 input views. As shown in Table 2, we found that there are performance gains when increasing the number of input views. However, the gain is marginal when comparing 9×9 views with 7×7 views. The 7×7 views shows the better performance in the mean square error. This shows the effectiveness of our view-shifting augmentation.

We also propose a rotation augmentation method for light field images. As in the depth estimation [24] and the optical flow estimation [8] using deep learning, the image rotation in the spatial dimension has been widely used as an augmentation technique. However, the conventional rotational method cannot be directly used, as it does not consider the directional characteristics of the light-field image. In the multi-stream part of our network, we extract features

Table 2. Effects of the angular resolutions and the augmentation techniques on performance.

Angular resolution	3×3	5×5	7×7					9×9
Augmentaion type	Full Aug	Full Aug	Color	Color + Viewshift	Color + Rotation	Color + scaling	Full Aug	Full Aug
Mean square error	1.568	1.475	2.799	2.564	1.685	2.33	1.434	1.461
Bad pixel ratio (>0.07px)	8.63	4.96	6.67	6.29	5.54	5.69	3.94	3.91

for epipolar property of viewpoint sets. To preserve this light field property, we first rotate sub-aperture images in the spatial dimension, and then rearrange the connection of the viewpoint sets and the streams as shown in Fig. 5. This rearrangement is necessary as the geometric properties change after the rotation. For example, pixels in the vertical direction are strongly related to each other in the vertical views as mentioned in Section 3.1. If we rotate the sub-aperture images in the vertical viewpoints by 90 degrees, it makes the horizontal view network stream to look at vertical characteristics. Thus, the rotated sub-aperture images should be input to the vertical view stream.

We additionally use general augmentation techniques such as the scaling and the flipping. When the images are scales, the disparity values need to be also scaled accordingly. We tune the scales of both the image and the disparity by $1/N$ times ($N = 1, 2, 3, 4$). The sign of disparity is reversed when flipping the light field images. With these augmentation techniques: the view-shifting, rotation [90, 180, 270 degrees], image scaling [0.25, 1], color scaling [0.5, 2], randomly converting color to gray scale from [0, 1]; gamma value from [0.8, 1.2] and flipping, we can increase the training data up to 288 times the original data.

We validate the effectiveness of the light-field specific augmentations. As seen in Table 2, there are large performance gains when using the rotation and flipping. We also observe that the scaling augmentation allows to cover various disparity ranges, which is useful for real light-field images with very narrow baselines. Through the augmentation techniques, we reduce disparity errors by more than 40%.

3.4. Details of learning

We exploit the patch-wise training by randomly sampling gray-scale patches of size 23×23 from the 16 synthetic light-field images [14]. To boost training speed, all convolutions in the layers are conducted without zero padding. We exclude some training data that contains reflection and refraction regions such as glass, metal and textureless regions, which result in incorrect correspondences. Reflection and refraction regions were manually masked out in Fig. 6. We also removed textureless regions where the mean absolute difference between a center pixel and other pixel in a patch is less than 0.02.

As the loss function in our network, we used the mean

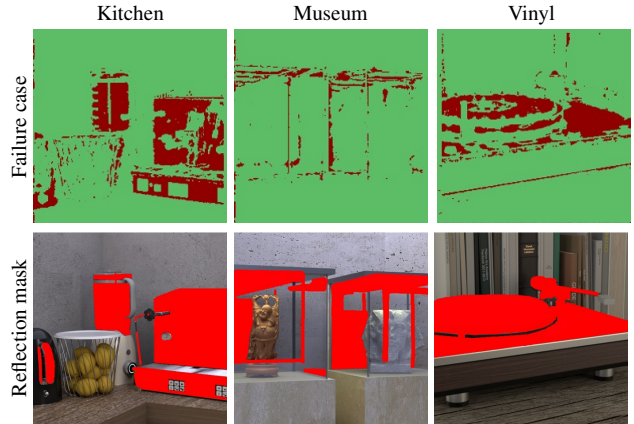


Figure 6. (Top) Failure cases in regions with reflections. (Bottom) Examples of reflection masks for training data.

absolute error (MAE) which is robust to outliers [9]. We use Rmsprop [32] optimizer and set the batch size to 16. The learning rate started at $1e-5$ and is decreased to $1e-6$. Our network takes 5~6 days to train on a NVIDIA GTX 1080TI and is implemented in TensorFlow [5].

4. Experiments

In this section, the performance of the proposed algorithm is evaluated using synthetic and real-world datasets. The 4D light field benchmark [14] was used for the synthetic experiments. The benchmark has 9×9 angular and 512×512 spatial resolutions. For real-world experiments, we utilized images captured with a Lytro illum [2].

4.1. Quantitative Evaluation

For the quantitative evaluation, we estimate the disparity maps using the test sets in the 4D Light Field Benchmark [14]. Bad pixel ratios and mean square errors were computed for the 12 light-field test images. Three thresholds (0.01, 0.03 and 0.07 pixels) for the bad pixel ratio are used, in order to better assess the performance of algorithms for difficult scenes.

In Fig. 7, we directly refer to the ranking tables, which are published on the benchmark website. Our EPINET shows the best performance in 3 out of 4 measures. Epinet-fcn is our EPINET model using the vertical, the horizontal, the left diagonal and the right diagonal viewpoints as input,

Bad pixel (Error<0.01)				Bad pixel (Error<0.03)				Bad pixel (Error<0.07)				Mean Square Error (multiplied with 100)			
Algorithm	Meta			Algorithm	Meta			Algorithm	Meta			Algorithm	Meta		
	MEDIAN	AVG	No preview		MEDIAN	AVG	No preview		MEDIAN	AVG	No preview		MEDIAN	AVG	No preview
Epinet-fcn-m	33.721	1	31.898	Epinet-fcn-m	7.731	1	9.537	OBER-cross+ANP	3.371	2	4.594	Epinet-fcn-m	1.203	1	2.418
Epinet-fcn9x9	35.863	2	32.982	Epinet-fcn	9.501	3	10.745	Epinet-fcn-m	2.996	1	4.646	Epinet-fcn	1.208	2	2.476
Epinet-fcn	37.520	4	34.988	Epinet-fcn9x9	9.058	2	11.212	Epinet-fcn	3.381	3	4.931	Epinet-fcn9x9	1.280	3	2.521
OBER-cross+ANP	36.812	3	35.226	OBER-cross+ANP	11.018	4	13.100	Epinet-fcn9x9	3.658	4	5.406	OBER-cross+ANP	1.464	5	2.584
OFSY_330/DNR	43.730	6	38.049	SPO-MO	15.243	5	14.258	SPO-MO	3.784	5	5.708	SPO-MO	1.805	7	3.518
SPO-MO	43.220	5	40.174	OBER-cross	15.465	6	18.731	CAE	8.711	10	8.211	CAE	2.667	11	3.730
OBER-cross	43.812	7	40.896	OFSY_330/DNR	20.373	8	20.225	SPO	8.779	11	8.466	FBS*	1.701	6	3.805
ZCTV	46.247	8	41.153	PS_RF	19.719	7	21.630	PS_RF	7.559	7	8.578	RM3DE	1.455	4	3.922
OBER	50.547	9	49.869	SPO	25.215	15	22.300	RPRF	9.892	13	10.020	SPO	3.309	15	3.968
*LF	59.187	10	54.466	GLFCV	23.479	11	22.450	RM3DE	7.992	8	10.216	OBER-cross	2.547	10	4.010
CAE	59.441	11	55.835	ZCTV	25.721	16	22.917	OBER-cross	6.715	6	10.289	OBER	2.381	9	4.616
GLFCV	60.506	12	57.876	CAE	23.386	10	22.949	EPN+OS+GC	8.594	9	10.724	PS_RF	2.169	8	4.617
RM3DE	63.521	15	58.079	RM3DE	23.561	12	23.259	OBER	9.021	12	11.677	RPRF	3.760	17	5.683
EPN+OS+GC	61.517	14	58.539	OBER	23.713	13	23.565	OFSY_330/DNR	11.329	17	12.036	RPRF-5view	3.295	14	5.944
SC_GC	60.601	13	61.701	EPN+OS+GC	21.731	9	23.828	GLFCV	10.759	15	12.196	*EPI1	3.932	18	5.975

Figure 7. Benchmark ranking (<http://hci-lightfield.iwr.uni-heidelberg.de>). Several versions of the proposed methods are highlighted.

Runtime (seconds)							
Algorithm	Meta			Algorithm	Meta		
	MEDIAN	AVG	No preview		MEDIAN	AVG	No preview
MVCMv0	0.110	1	0.111	*EPI1	85.045	15	88.194
Epinet-fcn	1.972	2	1.976	OBER-cross	96.200	16	96.417
Epinet-fcn9x9	2.032	3	2.041	OBER-cross+ANP	174.595	17	182.994
GLFCV	4.049	4	4.050	OFSY_330/DNR	198.299	18	200.282
BSL_I	4.640	5	5.456	EPN+OS+GC	260.602	19	274.710
BSL	5.149	6	5.962	LF_OCC	484.883	20	519.868
EPI2	8.789	7	8.406	FBS	680.850	21	655.905
Epinet-fcn-m	10.647	8	10.659	CAE	822.272	22	832.081
RPRF-5view	12.966	9	12.498	*LF	994.311	23	1009.756
RPRF	35.456	10	34.529	OMG_occ	1049.401	24	1163.938
ZCTV	37.400	11	37.450	PS_RF	1141.815	25	1412.623
OBER	40.420	12	40.141	SC_GC	2052.190	26	2056.344
*MV	45.638	14	40.879	SPO	2111.500	27	2115.417
RM3DE	45.149	13	47.434	SPO-MO	4297.000	28	4304.333

Figure 8. Runtime benchmark of the algorithms

Table 3. Quantitative evaluation of deep learning based methods using 50 synthetic LF images. The table provides the RMSE and MAE. For [12, 13], the error metrics are directly referred from [13].

Method (# of training images)	RMSE	MAE	Time
[12] (850)	1.87	1.13	35s
[13] (850)	0.83	0.34	0.8s
Ours (250)	0.14	0.036	0.93s

and Epinet-fcn9x9 is a model that uses all 9×9 viewpoints. The Epinet-fcn-m is a modified version of our Epinet-fcn. Epinet-fcn-m predicts multiple disparity maps by flipping and rotating (90, 180, 270 degrees) the given light field image. The final estimation is the average of the estimated disparity maps, which reduces the matching ambiguity. In addition to the accuracy, the EPINET is effectively the fastest algorithm among the state-of-the-art methods as shown in Fig. 8. Our computational time is second to MVCMv0, but its depth accuracy is the last in the benchmark.

Qualitative results (*Cotton*, *Boxes* and *Dots*) are shown in Fig. 10. The *Cotton* scene contains smooth surfaces, and the *Boxes* scene is composed of slanted objects with depth discontinuity occlusions. As can be seen from the examples, our EPINET reconstructs the smooth surface and

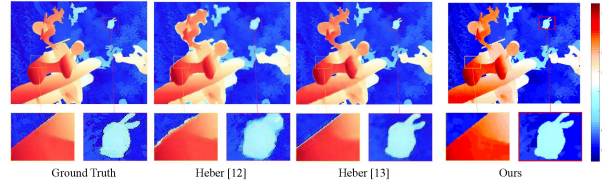


Figure 9. Comparison with deep learning-based methods [12, 13]. The results for [12, 13] are directly referred from [13].

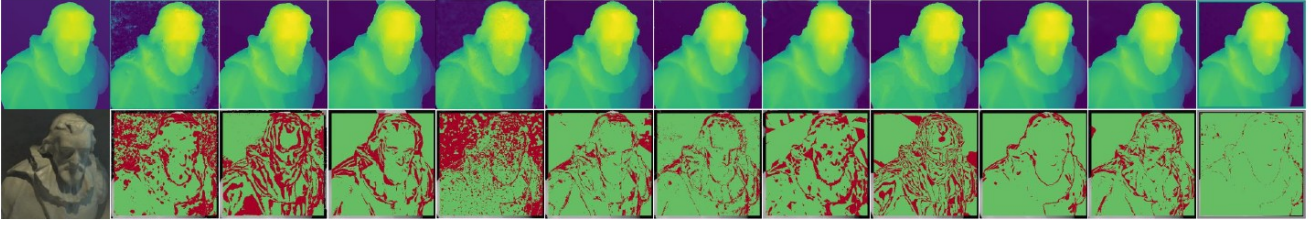
the sharp depth discontinuity better than previous methods. The EPINET infers accurate disparity values through the regression part in the network as our fully-convolutional layers can precisely distinguish the subtle difference of EPI slopes. The *Dots* scene suffers from image noise whose levels varies spatially. Once again, the proposed method achieves the best performance in this noisy scene because the 2×2 kernel has the effect of alleviating the noise effect.

A direct comparison between the EPINET and other state-of-the-art deep learning-based approaches [12, 13] can be found in Table 3 and Fig. 9. We trained the EPINET on 250 LF images provided by the authors of [12, 13] whose baseline is (-25, 5) pixels. The EPINET still outperforms the works in [12, 13]. Our multi-streams strategy to resolve the directional matching ambiguities enables to capture sharp object boundaries like the airplane's wing and the toy's head. Another reason for the better performance is that the LF images of [12, 13] contain highly textured regions with less noise compared to the HCI dataset.

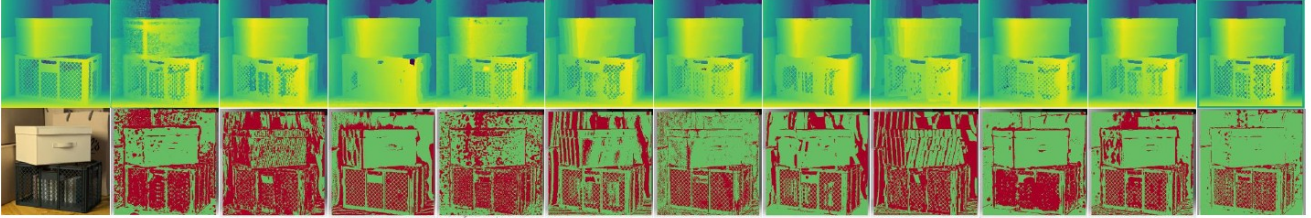
4.2. Real-world results

We demonstrate that our EPINET also achieves reliable results on real light-field images. We used the light-field images captured by a Lytro illum camera [2], provided by the authors of [6]. The real-world dataset is challenging as the data contain a combination of smooth and slanted surfaces with depth discontinuity. Additionally, these images suffer from severe image noise due to the inherent structural

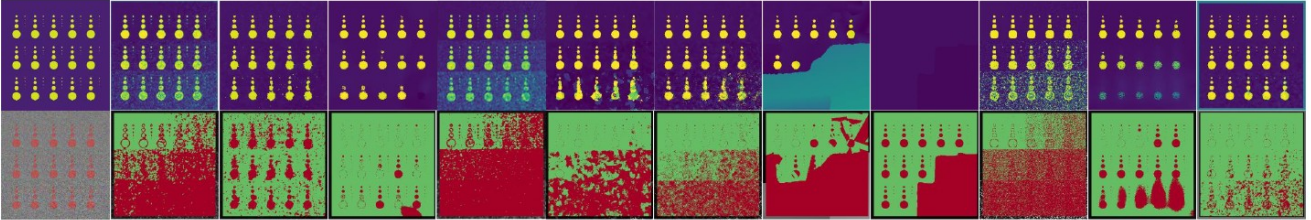
Cotton



Boxes

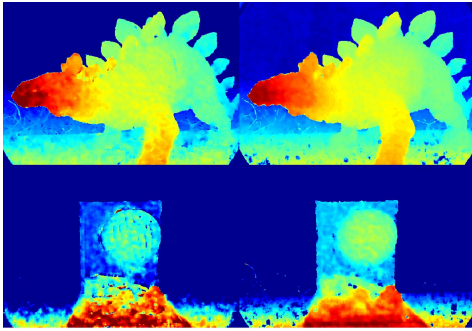


Dots



(a) GT (b) [36] (c) [33] (d) [16] (e) [18] (f) [39] (g) [43] (h) [27] (i) [15] (j) [29] (k) [17] (l) Ours

Figure 10. Qualitative results of the HCI light-field benchmark. Odd rows shows the estimated disparity results and even rows represent error maps for bad pixel ratio of 0.03.

(a) 7×7 (b) 9×9 Figure 11. Real world results using 7×7 angular resolution and 9×9 angular resolution of light field images.

problem in the camera. In Fig. 11, we compare the disparity predictions from the EPINET using the input viewpoints 7×7 and 9×9 . Although the performances of both EPINETs are similar in the synthetic data, there is a noticeable performance differences between the two in the real-world. In [37], it has been shown that the accuracy of the depth estimation from light field improves with more viewpoints, since they represent a consensus of all input views. Thus, we used the EPINET with 9×9 input viewpoints for the real-world experiments. We also remove sparse disparity errors using the conventional weighted median filter [23] for only the real-world dataset.



Figure 12. Mesh rendering result of our disparity. (unit: mm)

Fig. 13 compares qualitative results with previous methods. Although the work in [16] shows good results, the method requires several minutes for the depth estimation with careful parameter tuning. In contrast, our EPINET achieves the state-of-the-art results much faster, without any parameter tuning. An accurate disparity map can facilitate many applications. As an example, we reconstructed the 3D structure of an object captured by the Lytro illum camera in the metric scale using the depth computed with our method. In Fig. 12, the disparity map was converted into a 3D model in the metric scale using the calibration parameters estimated by the toolbox of [6]. The impressive results show that the proposed method can be used for further applications like the 3D printing.

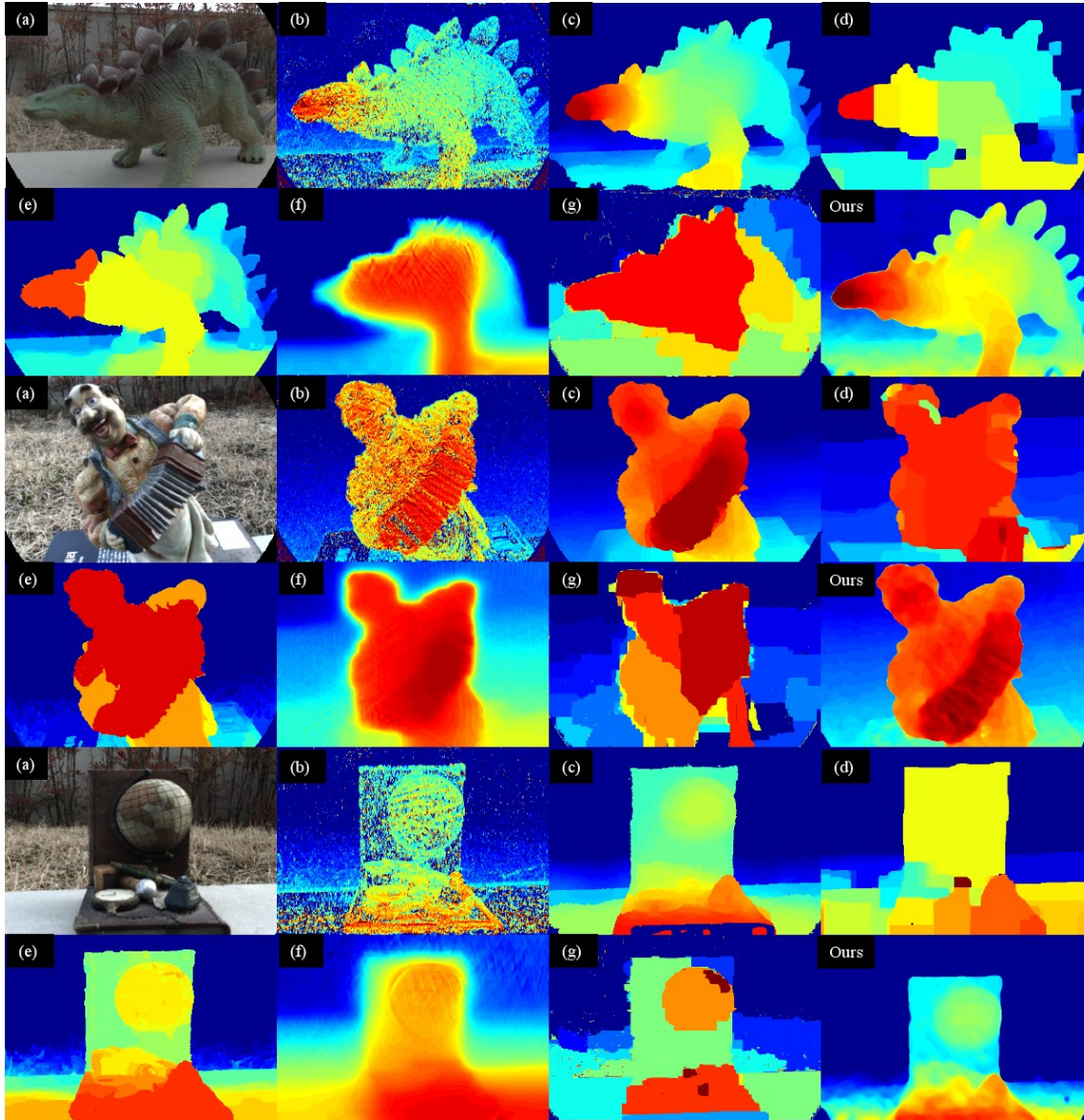


Figure 13. Qualitative results of real world data. (a) reference view (center view), (b) [36], (c) [16], (d) [39], (e) [33], (f) [31], (g) [42]

5. Conclusion

In this paper, we have proposed a fast and accurate depth estimation network using the light field geometry.

Our network has been designed taking into account the light field epipolar geometry to learn the angular and the spatial information using a combination of a multi-stream network and a merging network. In addition, we introduced light-field image-specific data augmentations such as view-shifting and rotation. Using the proposed method, we could overcome insufficient data problem and show the state-of-the-art results on the Benchmark light-field images as well as real-world light-field images.

There are still rooms for improving our method. First,

the easiest way to improve the CNN-based approach is to boost the number of realistic dataset. Second, our network fails to infer accurate disparities in reflection and textureless regions. To handle this issue, we think that a prior knowledge such as object material [35] can be included in the future work. We also expect that our network model can be improved by fusing a photometric cue [31] or a depth boundary cue [34].

Acknowledgement

This work was supported by the National Research Foundation of Korea (NRF) grant funded by the Korea government (MSIP) (NRF-2016R1A2B4014610).

References

- [1] Google inc., project tango. <https://www.google.com/atap/project-tango/>. 1
- [2] Lytro - illum. <https://illum.lytro.com/illum>. 1, 5, 6
- [3] The lytro camera. <http://www.lytro.com/>. 1
- [4] Microsoft inc., kinect 2. <https://www.microsoft.com/en-us/download/details.aspx?id=44561/>. 1
- [5] M. Abadi, A. Agarwal, P. Barham, E. Brevdo, Z. Chen, C. Citro, G. S. Corrado, A. Davis, J. Dean, M. Devin, S. Ghemawat, I. Goodfellow, A. Harp, G. Irving, M. Isard, Y. Jia, R. Jozefowicz, L. Kaiser, M. Kudlur, J. Levenberg, D. Mané, R. Monga, S. Moore, D. Murray, C. Olah, M. Schuster, J. Shlens, B. Steiner, I. Sutskever, K. Talwar, P. Tucker, V. Vanhoucke, V. Vasudevan, F. Viégas, O. Vinyals, P. Warden, M. Wattenberg, M. Wicke, Y. Yu, and X. Zheng. TensorFlow: Large-scale machine learning on heterogeneous systems, 2015. Software available from tensorflow.org. 5
- [6] Y. Bok, H.-G. Jeon, and I. S. Kweon. Geometric calibration of micro-lens-based light field cameras using line features. *IEEE Transactions on Pattern Analysis and Machine Intelligence (TPAMI)*, 39(2):287–300, 2017. 1, 6, 7
- [7] D. G. Dansereau, O. Pizarro, and S. B. Williams. Decoding, calibration and rectification for lenselet-based plenoptic cameras. In *Proceedings of IEEE Conference on Computer Vision and Pattern Recognition (CVPR)*, 2013. 1
- [8] A. Dosovitskiy, P. Fischer, E. Ilg, P. Hausser, C. Hazirbas, V. Golkov, P. van der Smagt, D. Cremers, and T. Brox. FlowNet: Learning optical flow with convolutional networks. In *Proceedings of IEEE Conference on Computer Vision and Pattern Recognition (CVPR)*, 2015. 3, 4
- [9] I. Goodfellow, Y. Bengio, and A. Courville. *Deep learning*. MIT press, 2016. 5
- [10] S. J. Gortler, R. Grzeszczuk, R. Szeliski, and M. F. Cohen. The lumigraph. In *Proceedings of ACM SIGGRAPH*, pages 43–54. ACM, 1996. 2
- [11] S. Heber and T. Pock. Shape from light field meets robust pca. In *Proceedings of European Conference on Computer Vision (ECCV)*, 2014. 1, 2
- [12] S. Heber and T. Pock. Convolutional networks for shape from light field. In *Proceedings of IEEE Conference on Computer Vision and Pattern Recognition (CVPR)*, 2016. 2, 6
- [13] S. Heber, W. Yu, and T. Pock. Neural epi-volume networks for shape from light field. In *Proceedings of International Conference on Computer Vision (ICCV)*, 2017. 2, 6
- [14] K. Honauer, O. Johannsen, D. Kondermann, and B. Goldluecke. A dataset and evaluation methodology for depth estimation on 4d light fields. In *Proceedings of Asian Conference on Computer Vision (ACCV)*, 2016. 2, 4, 5
- [15] C.-T. Huang. Robust pseudo random fields for light-field stereo matching. In *Proceedings of IEEE Conference on Computer Vision and Pattern Recognition (CVPR)*, 2017. 1, 7
- [16] H.-G. Jeon, J. Park, G. Choe, J. Park, Y. Bok, Y.-W. Tai, and I. S. Kweon. Accurate depth map estimation from a lenslet light field camera. In *Proceedings of IEEE Conference on Computer Vision and Pattern Recognition (CVPR)*, 2015. 1, 2, 7, 8
- [17] H.-G. Jeon, J. Park, G. Choe, J. Park, Y. Bok, Y.-W. Tai, and I. S. Kweon. Depth from a light field image with learning-based matching costs. *IEEE Transactions on Pattern Analysis and Machine Intelligence*, PP(99):1–14, Jan. 2018. 7
- [18] O. Johannsen, A. Sulc, and B. Goldluecke. What sparse light field coding reveals about scene structure. In *Proceedings of IEEE Conference on Computer Vision and Pattern Recognition (CVPR)*, 2016. 2, 3, 7
- [19] N. K. Kalantari, T.-C. Wang, and R. Ramamoorthi. Learning-based view synthesis for light field cameras. *ACM Transactions on Graphics (TOG)*, 35(6):193, 2016. 2
- [20] M. Levoy and P. Hanrahan. Light field rendering. In *Proceedings of ACM SIGGRAPH*, pages 31–42. ACM, 1996. 2
- [21] J. Long, E. Shelhamer, and T. Darrell. Fully convolutional networks for semantic segmentation. In *Proceedings of IEEE Conference on Computer Vision and Pattern Recognition (CVPR)*, pages 3431–3440, 2015. 3
- [22] W. Luo, A. G. Schwing, and R. Urtasun. Efficient deep learning for stereo matching. In *Proceedings of IEEE Conference on Computer Vision and Pattern Recognition (CVPR)*, 2016. 3
- [23] Z. Ma, K. He, Y. Wei, J. Sun, and E. Wu. Constant time weighted median filtering for stereo matching and beyond. In *Proceedings of International Conference on Computer Vision (ICCV)*, 2013. 7
- [24] N. Mayer, E. Ilg, P. Hausser, P. Fischer, D. Cremers, A. Dosovitskiy, and T. Brox. A large dataset to train convolutional networks for disparity, optical flow, and scene flow estimation. In *Proceedings of IEEE Conference on Computer Vision and Pattern Recognition (CVPR)*, 2016. 4
- [25] R. Ng, M. Levoy, M. Brédif, G. Duval, M. Horowitz, and P. Hanrahan. Light field photography with a handheld plenoptic camera. *Computer Science Technical Report CSTR*, 2(11), 2005. 1
- [26] Raytrix. 3d light field camera technology. <http://www.raytrix.de/>. 1
- [27] L. Si and Q. Wang. Dense depth-map estimation and geometry inference from light fields via global optimization. In *Proceedings of Asian Conference on Computer Vision (ACCV)*, 2016. 7
- [28] P. P. Srinivasan, T. Wang, A. Sreelal, R. Ramamoorthi, and R. Ng. Learning to synthesize a 4d rgb-d light field from a single image. In *Proceedings of International Conference on Computer Vision (ICCV)*, 2017. 2
- [29] M. Strecke, A. Alperovich, and B. Goldluecke. Accurate depth and normal maps from occlusion-aware focal stack symmetry. In *Proceedings of IEEE Conference on Computer Vision and Pattern Recognition (CVPR)*, 2017. 3, 7
- [30] M. W. Tao, S. Hadap, J. Malik, and R. Ramamoorthi. Depth from combining defocus and correspondence using light-field cameras. In *Proceedings of International Conference on Computer Vision (ICCV)*, 2013. 1, 2
- [31] M. W. Tao, P. P. Srinivasan, S. Hadap, S. Rusinkiewicz, J. Malik, and R. Ramamoorthi. Shape estimation from shading, defocus, and correspondence using light-field angular

- coherence. *IEEE Transactions on Pattern Analysis and Machine Intelligence (TPAMI)*, 39(3):546–559, 2017. 2, 8
- [32] T. Tieleman and G. Hinton. Lecture 6.5-rmsprop: Divide the gradient by a running average of its recent magnitude. *COURSERA: Neural networks for machine learning*, 4(2):26–31, 2012. 5
- [33] T.-C. Wang, A. Efros, and R. Ramamoorthi. Occlusion-aware depth estimation using light-field cameras. In *Proceedings of International Conference on Computer Vision (ICCV)*, 2015. 7, 8
- [34] T.-C. Wang, A. A. Efros, and R. Ramamoorthi. Depth estimation with occlusion modeling using light-field cameras. *IEEE Transactions on Pattern Analysis and Machine Intelligence (TPAMI)*, 38(11):2170–2181, 2016. 1, 2, 8
- [35] T.-C. Wang, J.-Y. Zhu, E. Hiroaki, M. Chandraker, A. A. Efros, and R. Ramamoorthi. A 4d light-field dataset and cnn architectures for material recognition. In *Proceedings of European Conference on Computer Vision (ECCV)*, 2016. 2, 8
- [36] S. Wanner and B. Goldluecke. Globally consistent depth labeling of 4D lightfields. In *Proceedings of IEEE Conference on Computer Vision and Pattern Recognition (CVPR)*, 2012. 7, 8
- [37] S. Wanner and B. Goldluecke. Variational light field analysis for disparity estimation and super-resolution. *IEEE Transactions on Pattern Analysis and Machine Intelligence (TPAMI)*, 36(3):606–619, 2014. 1, 2, 3, 7
- [38] B. Wilburn, N. Joshi, V. Vaish, E.-V. Talvala, E. Antunez, A. Barth, A. Adams, M. Horowitz, and M. Levoy. High performance imaging using large camera arrays. *ACM Transactions on Graphics (TOG)*, 24(3):765–776, 2005. 1
- [39] W. Williem and I. Kyu Park. Robust light field depth estimation for noisy scene with occlusion. In *Proceedings of IEEE Conference on Computer Vision and Pattern Recognition (CVPR)*, 2016. 2, 7, 8
- [40] Y. Yoon, H.-G. Jeon, D. Yoo, J.-Y. Lee, and I. S. Kweon. Light field image super-resolution using convolutional neural network. *IEEE Signal Processing Letters*, 24(6):848–852, Feb. 2017. 2
- [41] Y. Yoon, H.-G. Jeon, D. Yoo, J.-Y. Lee, and I. So Kweon. Learning a deep convolutional network for light-field image super-resolution. In *Proceedings of International Conference on Computer Vision Workshop (ICCVW)*, pages 24–32, 2015. 2
- [42] Z. Yu, X. Guo, H. Ling, A. Lumsdaine, and J. Yu. Line assisted light field triangulation and stereo matching. In *Proceedings of International Conference on Computer Vision (ICCV)*, 2013. 1, 8
- [43] S. Zhang, H. Sheng, C. Li, J. Zhang, and Z. Xiong. Robust depth estimation for light field via spinning parallelogram operator. *Computer Vision and Image Understanding (CVIU)*, 145:148–159, 2016. 1, 2, 3, 7